Volume 3
Number 15
7 August 2022
Pages 6073–6386

Materials Advances

rsc.li/materials-advances

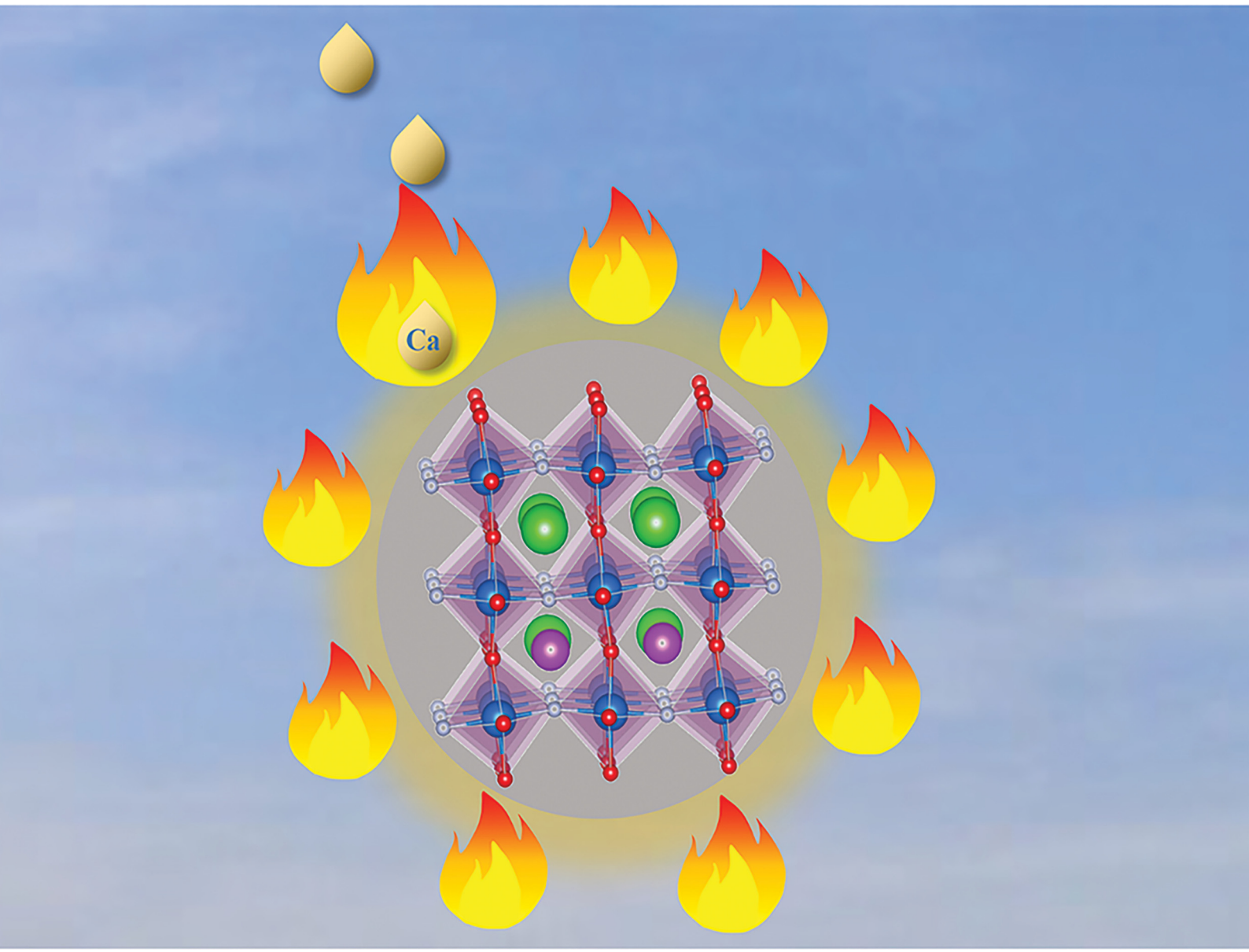

ISSN 2633-5409

ROYAL SOCIETY OF CHEMISTRY

PAPER

Tao Han, Damir Valiev *et al.*

A green emitting (Ba,Ca)ScO_2F:Bi^{3+},K^+ perovskite phosphor with high efficiency and good thermal stability for LED backlight displays

Materials Advances

ROYAL SOCIETY OF CHEMISTRY

PAPER

View Article Online
View Journal | View Issue

Cite this: *Mater. Adv.*, 2022, 3, 6171

A green emitting (Ba,Ca)ScO_2F:Bi^{3+},K^+ perovskite phosphor with high efficiency and good thermal stability for LED backlight displays†

Mingsheng Cai,[ab] Tianchun Lang,[a] Tao Han, *[a] Damir Valiev, *[b] Shuangqiang Fang,[c] Houjiang You,[a] Bitao Liu,[a] Ling Du,[a] Zichao Xu[a] and Elena F. Polisadova[b]

Received 12th May 2022,
Accepted 13th June 2022

DOI: 10.1039/d2ma00531j

rsc.li/materials-advances

Investigating narrow-band green emitting phosphors with high efficiency and good thermal stability is the main goal of the present light-emitting diode (LED) display research. Here, $Ba_{1-x}Ca_xScO_2F$:0.001Bi^{3+},0.001K^+ (x = 0–0.12) perovskite phosphors, emitting narrow green light excited by a 415 nm chip, were developed using the cation substitution design strategy. The effects of Ca^{2+} substitution for Ba^{2+} in the $Ba_{1-x}Ca_xScO_2F$:0.001-Bi^{3+},0.001K^+ crystal structures and photoluminescence properties were investigated. All the phosphors show the cubic perovskite-type structure in the space group *Pm3m*. The evolution of the cell parameters and the Ba/Ca/K/Bi–O bond lengths were evaluated. The phosphors with the internal quantum efficiency of 77.4% exhibit bright green emission peaking at 510 nm under 415 nm chip excitation. The improvement of luminescence efficiency and thermal stability was discussed in detail in relation to the local structure variation. The cation substitution design strategy mentioned here can become an important approach to realize the spectral modulation through controlling the micro-environment in the lattice for excellent LED backlight displays.

Introduction

Nowadays, the phosphor-converted white light emitting diodes (pc-wLEDs) as promising devices for backlight displays have attracted great attention. As new-generation solid-state lighting sources, they have excellent performance compared with the traditional lighting, such as long lifetime, good stability, energy conservation, high luminous efficiency, environmental protection, and so on.[1–7]

For backlight displays, the most popular way of preparing w-LEDs is by combining a blue InGaN LED chip and a YAG:Ce^{3+} yellow emitting phosphor and a nitride $(Sr,Ca)_2Si_5N_8$:Eu^{2+} red emitting phosphor.[8–10] However, the over-large full-width at half-maximum (FWHM) values of YAG:Ce^{3+}(>100 nm) and $(Sr,Ca)_2Si_5N_8$:Eu^{2+}(>90 nm) limit their applications. Meanwhile, the color gamut of the backlights can reach only ~80% of the National Television System Committee (NTSC) standard in the CIE 1931 standard system due to the lack of green emission. Nevertheless, the deficient green emission reduces the vividness of the colors.[9] Therefore, it is extremely necessary to explore a high-efficiency narrow band green emitting phosphor with excellent thermal stability.

To meet the requirements of backlighting technologies, various green emitting phosphors have been developed for improvement of the color gamut.[10] For example, the green emitting phosphors Sr_2SiO_4:Eu^{2+} (the color gamut – 74.7% of the NTSC value),[11] β-sialon:Eu^{2+} (Color Gamnt – 82.1% of the NTSC value)[12] and $SrGa_2S_4$:Eu^{2+} (Color Gamnt – 83.8% of the NTSC value)[13] are mixed with nitride $(Sr,Ca)_2Si_5N_8$:Eu^{2+}, a red emitting phosphor, and used for LED displays. It is worth noting that the highest color gamut of the fabricated device is <90% of the NTSC value, which does not significantly improve the color gamut.

The cation substitution design is an efficient route to develop phosphors with high-quality photoluminescence properties. The benefits vary from red/blue-shift tuning of the emission peak position, to improved luminescence efficiency or thermal stability.[14–26] For example, the energy transfer of Ce^{3+} → Mn^{2+} ions in $(Lu_{1-x}Y_x)_3Al_{4.8}Si_{0.2}O_{12}$:0.1$Ce^{3+}$,0.2$Mn^{2+}$ garnet solid solution can be affected by the replacement of Y^{3+} ions for Lu^{3+} ions, and this is attributed to the reduction of the distance between Ce^{3+} and Mn^{2+} ions in the dodecahedron.[27] The emission band shift towards the longer

[a] *Chongqing Key Laboratory of Materials Surface & Interface Science, Research Institute for New Materials Technology, Chongqing University of Arts and Sciences, Chongqing, 402160, China. E-mail: danbaiht@126.com*
[b] *School of Advanced Manufacturing Technologies, National Research Tomsk Polytechnic University, Tomsk, 634050, Russia*
[c] *College of Optical and Electronic Technology, China Jiliang University, Hangzhou, 310018, China*

† Electronic supplementary information (ESI) available. See DOI: https://doi.org/10.1039/d2ma00531j

wavelengths can be achieved through the Ca/Ba substitution in the $Ba_2MgSi_2O_7$:Eu^{2+} host, as a result of the increase of the Eu^{2+} 5d electron crystal field splitting.[28] The valence band of the host lattice can be optimized by Sr^{2+} substitution for Ba^{2+} in Ba_2SiO_4:Eu^{2+} due to the enhancement of the structural rigidity and the improvement of the thermal emission stability.[29] In most cases, the cation substitution design can obtain phosphors with optimized photoluminescence properties.

In this contribution, we report a phosphor having maximum excitation wavelength at 415 nm and a bright green emission. The compositions, $Ba_{1-x}Ca_xScO_2F$:Bi^{3+},K^+ (x = 0–0.12), were developed by the cation substitution design strategy starting from $BaScO_2F$:Bi^{3+},K^+.[14] A series of $Ba_{1-x}Ca_xScO_2F$:Bi^{3+},K^+ (x = 0–0.12) phosphors were synthesized by substitution of smaller Ca^{2+} ions for Ba^{2+} ions. Their structural evolution, morphology, absorption spectra, luminescence properties, temperature-dependent luminescence properties, and LED backlight performance were systemically investigated. The effects of micro-structure adjustment on enhancement of the luminescence intensity, red shift of the emission band and thermal stability improvement were discussed in detail. In addition, using the synthesized phosphor as a green emitter, a w-LED device with a high color gamut of 110% of the NTSC value was realized, showing good potential applications in backlight displays.

Experimental

Materials and synthesis

$Ba_{1-x}Ca_xScO_2F$:0.001Bi^{3+},0.001K^+ (x = 0, 0.03, 0.06, 0.09, and 0.12) phosphor powders were prepared by the high-temperature solid-state reaction method. Typically, $BaCO_3$ (99.99%, Aladdin), BaF_2 (99.99%, Aladdin), Sc_2O_3 (99.99%, Aladdin), $CaCO_3$ (99.99%, Aladdin), Bi_2O_3 (99.99%, Aladdin) and K_2CO_3 (99.99%, Aladdin) powders were stoichiometrically mixed together. Then, the mixtures were calcined at 1200 °C for 8 h in a box furnace. After that, the pretreatment samples were calcined at 1100 for 4 h in a reductive atmosphere (H_2 10% + N_2 90%) gas mixture to achieve the trivalent state for Bi ions, as shown in Fig. S1 (ESI†). The resulting products were slowly cooled and crushed finely into powders for further characterization.

Characterization methods

The crystal structures of the samples were characterized by using X-ray diffractometry (XRD, TD-3500, Dandong, China) using Cu-Kα radiation (λ = 1.5406 Å) and the cathode voltage and tube current were 30 kV and 20 mA, respectively. The structural refinements were done by the GSAS program. The microstructures and elemental compositions of the samples were characterized by scanning electron microscopy (SEM, FeHelios NanoLab 600i) and energy dispersive spectrometry (EDS, Oxford Instruments). The absorption spectra of the samples in the spectral range of 200–800 nm were measured by a UV-VIS-NIR spectrophotometer (Cary 5000, Varian Inc.). The photoluminescence (PL) spectra and PL excitation spectra (PLE) were measured by using a fluorescent spectrophotometer (F-7000, Hitachi, Japan) with a 150W Xe lamp at room temperature. The internal quantum efficiencies were obtained using an F-7000 with a Quanta-φ integrating sphere and a polytetrafluoroethylene sample cup. The temperature-dependent luminescence properties were measured by an FLS980 spectrometer (Edinburgh Instruments, the United Kingdom) with a 450 W Xe lamp as the excitation source. The lifetimes were measured by an FLS920 spectrometer (Edinburgh, UK) equipped with a nanosecond flash lamp as the excitation source. The photoelectric properties of the fabricated w-LEDs, including the PL spectra, CIE color coordinates, and CRI, were measured by using the integrating sphere (HSP6000 spectroscopic analysis system, Hangzhou, China) technique.

LED fabrication

The w-LEDs were fabricated from a mixture of a transparent silicone resin with $Ba_{0.94}Ca_{0.06}ScO_2F$:0.001Bi^{3+},0.001K^+ phosphor and commercial $CaAlSiN_3$:Eu^{2+} phosphor. After removing the bubbles through the vacuum treatment, the prepared mixture was coated on a 415 nm NUV chip and then heated at 100 °C for 1 h and 150 °C for 3 h.

Results and discussion

Phase characterization and crystal structure

The XRD patterns for all $Ba_{1-x}Ca_xScO_2F$:0.001Bi^{3+},0.001K^+ (x = 0, 0.03, 0.06, 0.09, and 0.12) powders are shown in Fig. 1a. It is clear that all diffraction peaks are well consistent with those of $BaScO_2F$ (ICSD #150171 standard card),[14] implying the pure phase formation (Fig. 1a). Hence, the main phase structure does not change by co-doping Bi^{3+},K^+, and Ca^{2+}, successfully gaining the expected phosphors.

With the increase of the Ca^{2+} concentration, all the diffraction peaks shift to larger angles (Fig. 1b) due to the smaller ionic radius of Ca^{2+} (1.34 Å) replacing Ba^{3+} (1.61 Å). These changes in XRD patterns could be explained by the Bragg equation:[27]

$$2d \sin\theta = n\lambda \quad (1)$$

where d is the interplanar spacing, λ is the X-ray wavelength, and θ is the diffraction angle. Namely, the Ba^{2+} ions are replaced by smaller Ca^{2+} ions, leading to the shrinkage of the unit cell and the decrease of the spacing. To investigate crystal structure disorder caused by doping Ca^{2+}, the Rietveld refinements of the XRD patterns are performed, as presented in Fig. 1b. The refined crystallographic parameters of the $Ba_{1-x}Ca_xScO_2F$:Bi^{3+},K^+ (x = 0, 0.03, 0.06, 0.09, and 0.12) samples are shown in Table 1. The residual factors (R) of the refinement converge to a low level, indicating that the refinement results are reliable and stable. The cell parameters and the cell volume V decrease linearly with the increase of the doping concentration of Ca^{2+}. Moreover, the bond lengths of d(Ba/Ca/Bi/K–O/F) decrease from 2.9490(4) Å to 2.9440(5) Å with increasing x, as shown in Fig. 1f. It is indicated that the doping of Ca^{2+} ions has

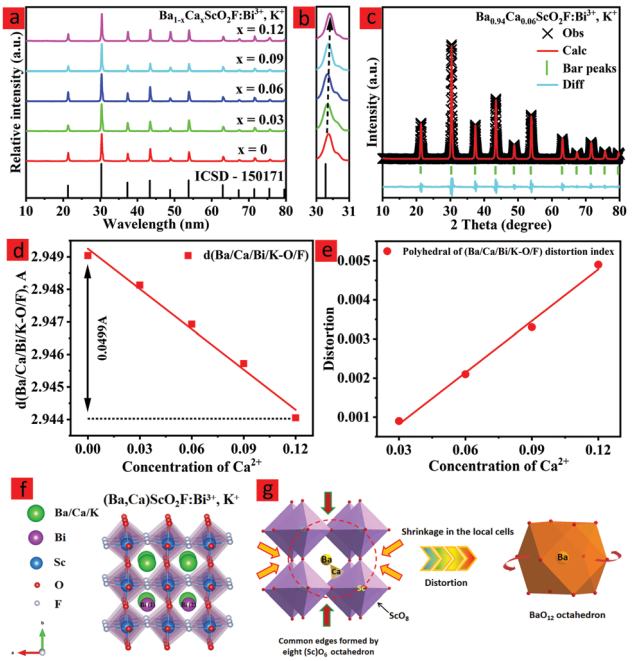

Fig. 1 XRD patterns (a) with the enlarged patterns in the region of 30–31° (b), and X-ray Rietveld refinement (c). Bond length d(Ba/Ca/Bi/K–O/F) change with increasing x (d). Distortion index of the (Ba/Ca/Bi/K)O12 polyhedron change with increasing x (e). Crystal structure (f) of the $Ba_{1x}Ca_xScO_2F$:0.001Bi^{3+},0.001K^+ (x = 0–0.12) phosphors. Influence of Ca^{2+} ion doping on the local coordination environment around BaO12 in $Ba_{0.94}Ca_{0.06}ScO_2F$:0.001Bi^{3+},0.001K^+ (g).

an obvious influence on the $(Ba/Ca/Bi/K)O_{12}$ polyhedron, which exhibits a shrinkage of the unit cell with increasing concentration of Ca^{2+}, resulting in the shorter bond lengths d(Ba/Ca/Bi/K–O). Hence, the variation of bond length (Bi–O) causes the distortion of the $[BiO_{12}]$ polyhedra and changes the local crystal field strength of Bi^{3+}. The small displacement of the polyhedra can be in the conformation of asymmetric contracting, twisting and bending types, resulting in different degrees of polyhedral distortion.[30] The distortion of the BiO_{12} polyhedra is attributed to the asymmetric contracting of the (Bi–O) bonds. Consequently, the polyhedral distortion index (D) can be calculated by the following equation:[31]

$$D = \frac{1}{n}\sum_{i=1}^{n}\frac{|d_i - d_{av}|}{d_{av}} \quad (2)$$

where d_i represents the distance from the central atom to the i-th coordinating atom and d_{av} represents the average length of all the bonds. As shown in Fig. 1g, the results present that the polyhedral distortion index linearly increases from 0.0009 to 0.0049 with the increase of Ca^{2+} concentration. As it is known, the increase of the polyhedral distortion of BiO_{12} can increase the crystal field splitting of Bi^{3+}, which leads to a smaller $^1S_0$–$^3P_1$ energy level displacement.

Fig. 1d presents the crystal structure of (Ba,Ca)ScO_2F:0.001-Bi^{3+},0.001K^+, which shows that the unit cell is composed of corner-connected $[Sc(O/F)_6]$ with the Ba/Ca/Bi/K cation sitting in the octahedral cavity with cuboctahedral $[Ba/Ca/Bi/K(O/F)_{12}]$ coordination. The anion sublattice is composed of disordered oxygen and fluorine in an approximate 67% : 33% ratio.[32]

To prove the replacement relationship of Ca^{2+} in the host, the acceptable percentage difference in the ionic radius between the doped and substituted ions should not exceed 25% based on the defect chemistry.[33] The replacement relation can be calculated by the following equation:[33]

$$D_r = 100 \times \frac{[R_m(CN) - R_d(CN)]}{R_m(CN)} \quad (3)$$

where D_r represents the radius percentage difference, R_m and R_d are the radii of the host cation and the doped ion, respectively, and CN represents the coordination number. As we know, the ionic radius of dopant Ca^{2+} (rCa^{2+} = 1.34 Å, coordination number (CN) = 12) is similar to Ba^{2+} (rBa^{2+} = 1.61 Å, CN = 12)[34] and the value of the radius percentage discrepancy between Ba^{2+} and Ca^{2+} is 16.6%, which is less than the limiting value. Hence, Ca^{2+} ions can be doped into the $BaScO_2F$ host to replace Ba^{2+} sites, as shown in Fig. 1e.

The HR-TEM patterns of $BaScO_2F$:Bi^{3+},K^+ and $Ba_{0.94}Ca_{0.06}ScO_2F$:Bi^{3+},K^+ are demonstrated in Fig. 2. $Ba_{0.94}Ca_{0.06}ScO_2F$:-Bi^{3+},K^+ has a relatively high crystallinity relative to that of $BaScO_2F$:Bi^{3+},K^+. Fig. 1(e and f) show the elemental mapping images, demonstrating that the Ba, Ca, Sc, O, F, Bi and K elements are uniformly distributed over the $BaScO_2F$ particles, which indicates that the Ca^{2+}, Bi^{3+} and K^+ are successfully incorporated into the crystal lattice.

Photoluminescence properties

To investigate the influence of Ca^{2+} replacing Ba^{2+} on the luminescence properties in the host, the PL excitation and PL spectra of $Ba_{1-x}Ca_xScO_2F$:Bi^{3+},K^+ (x = 0, 0.03, 0.06, 0.09, and 0.12) were measured, as shown in Fig. 3(a and b). The PL excitation spectra indicate that there are two obvious absorption bands peaking at 360 and 415 nm, as observed by monitoring at 506 nm. The peaks at 360 and 415 nm are attributed

Table 1 Refined results and structural parameters of the $Ba_{1-x}Ca_xScO_2F$:Bi^{3+},K^+ (x = 0, 0.03, 0.06, 0.09, and 0.12)

Refined formula	x = 0	x = 0.03	x = 0.06	x = 0.09	x = 0.12
Crystal system	Cubic	Cubic	Cubic	Cubic	Cubic
Space group	*Pm3m*	*Pm3m*	*Pm3m*	*Pm3m*	*Pm3m*
Cell parameter (Å)	4.1678(8)	4.1675(4)	4.1671(6)	4.1664(1)	4.1655(7)
Volume (Å^3)	72.441(6)	72.421(4)	72.401(3)	72.386(5)	72.364(7)
Bond length (Ba/Ca/Bi/K–O/F)	2.9490(4)	2.9481(3)	2.9469(3)	2.9457(2)	2.9440(5)
U_{iso} (Ba) (Å^2)	0.0130(7)	—	0.0104(2)	—	—
R_p	6.37%	6.48%	6.54%	6.62%	6.73%
R_{wp}	9.22%	9.31%	9.47%	9.52%	9.61%

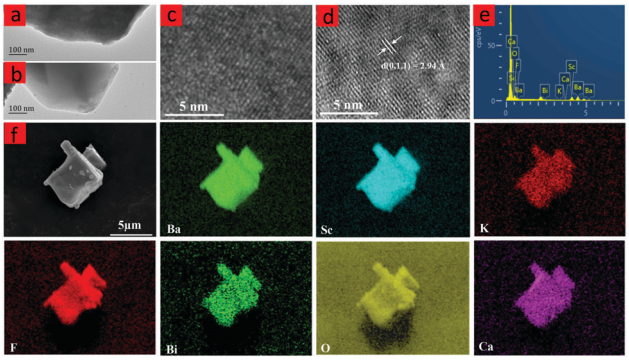

Fig. 2 TEM images of the $BaScO_2F$:0.001Bi^{3+},0.001K^+ (a) and $Ba_{0.94}Ca_{0.06}ScO_2F$:0.001Bi^{3+},0.001K^+ (b). HRTEM images of the $BaScO_2F$:0.001Bi^{3+},0.001K^+ (c) and $Ba_{0.94}Ca_{0.06}ScO_2F$:0.001Bi^{3+},0.001K^+ (d). EDS spectrum and the element mapping images of a phosphor (e and f).

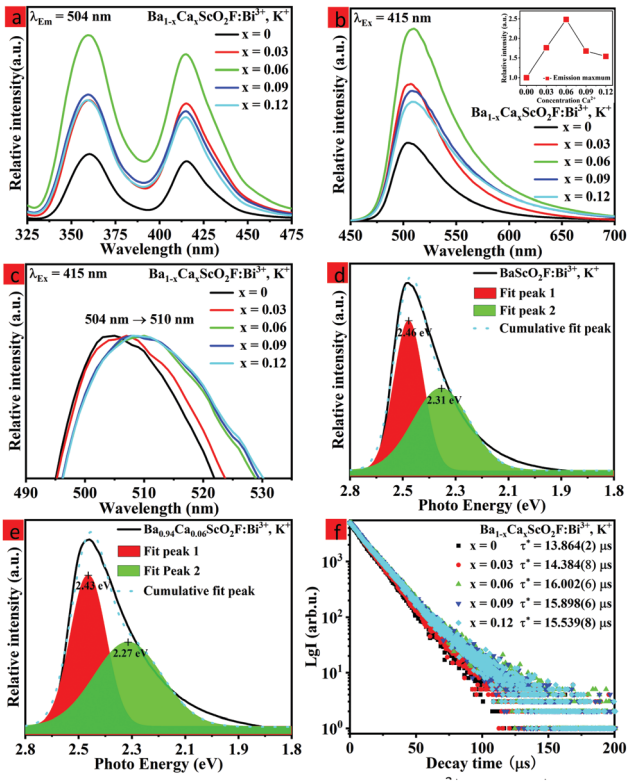

Fig. 3 The PLE spectra of $Ba_{1-x}Ca_xScO_2F$:0.001Bi^{3+},0.001K^+ (x = 0, 0.03, 0.06, 0.09, and 0.12) samples monitored at 504 nm (a). The PL spectra of $Ba_{1-x}Ca_xScO_2F$:0.001Bi^{3+},0.001K^+ (x = 0, 0.03, 0.06, 0.09, and 0.12) under 415 nm excitation (b). The inset shows the intensities of the peaks at 510 nm. The PL emission spectra (λ_{ex} = 415 nm) showing the red shift with increasing Bi^{3+} contents (c). Gaussian fitting of the PL spectra of $Ba_{1-x}Ca_xScO_2F$:0.001Bi^{3+},0.001K^+ (x = 0, 0.06, and 0.12) under 415 nm excitation (d and e). Room temperature decay curves, as recorded under excitation at 415 nm and monitored at 510 nm (f).

to the transitions of Bi^{3+} from the ground state $^1S_0$ to $^1P_1$ and $^3P_1$ excited states, respectively.[33] The emission spectra show bright cyan emission from 430 to 750 nm, as the sample is excited at 415 nm, which is ascribed to the transition of Bi^{3+} from $^3P_1$ to $^1S_0$.[35–37] The emission spectrum shape of Bi^{3+} does not obviously change, but the peak position and the PL intensity of the emission spectrum regularly change on the replacement of Ca^{2+} ions for Ba^{2+} ions. With increasing x, the PL intensity of the maximum at 510 nm first increases and then quenches. The maximal intensity of emission is increased to 2.5 times when x = 0.06 compared to the phosphor composition with x = 0. This is possible due to the small atomic size Ca^{2+} ions that substitute for Ba^{2+} ions with bigger atomic size. The luminescence efficiencies of the $Ba_{1-x}Ca_xScO_2F$:Bi^{3+},K^+ phosphors are enhanced due to the lattice shrinkage effect that reduces the non-radiative relaxation process and the rigidity of $BaScO_2F$ structure frameworks is improved. However, when a large amount of Ba^{2+} are replaced by Ca^{2+}, the photoluminescence intensity decreases due to the formation of defect energy levels.[38–41] The measured internal quantum efficiencies of $Ba_{1-x}Ca_xScO_2F$:Bi^{3+},K^+ (x = 0, 0.06) are 54.3% (x = 0) and 77.4% (x = 0.06) (Fig. 3b), respectively, under excitation by 415 nm at room temperature.

With increasing Ca^{2+} substitution for Ba^{2+}, the emission bands show an obvious red shift from 504 to 510 nm, as represented in Fig. 3c. The red shift is attributed to the decreasing of the cell volume (or lattice parameters) and the crystal lattice shrinkage that usually causes a strong crystal field splitting. As we know, the slight variation of the bond length for the Bi^{3+} coordination environment with the Ca^{2+} content increase can lead to a change of the Bi $^3P_1$ orbital splitting, the Stokes shift, and the centroid shift. Therefore, it is significant to discuss the change of the crystal field, which can be analyzed through the equation:[14]

$$D_q = \frac{Ze^2r^4}{6R^5} \quad (4)$$

where D_q represents the splitting energy, Z refers to the anionic charge, e denotes the electron charge, r represents the radius of the d-wave function, and R is the bond length between the luminescent cation and its ligand. Eqn (4) indicates that the crystal field splitting D_q is mainly dependent on the bond length R.[42] When Ba^{2+} ions are replaced by Ca^{2+} ions, the average bond length R is decreased resulting in a larger crystal field splitting. Hence, the red shift of the emission band is attributed to the enhancement of the crystal splitting of P orbitals of Bi^{3+} ions.[43,44] Furthermore, the symmetry is decreased with the incorporation of the doping ions and it affects the preferential orientation of a Bi^{3+} P orbital, so that the Bi^{3+} emission shifts to a longer wavelength.

The decay time of the phosphor is dependent on the activator radiation and the non-radiation transition process.[28] Therefore, the luminescence decay kinetics can be clarified by analysis of the decay curves. Fig. 3f shows the decay curves of the $Ba_{1-x}Ca_xScO_2F$:Bi^{3+},K^+ (x = 0, 0.03, 0.06, 0.09, and 0.12) samples monitored at 510 nm at room temperature. The decay curves can be approximated by the double-exponential

function:[22]

$$I(t) = I_0 + A_1 \exp\left(\frac{-t}{\tau_1}\right) + A_2 \exp\left(\frac{-t}{\tau_2}\right) \quad (5)$$

where t represents the time, $I(t)$ is the luminescence intensity at that time, A_1 and A_2 are the fitting constants, and τ_1 and τ_2 represent the decay times for the corresponding exponential components. The value of the average lifetime τ^* can be expressed as:[22]

$$\tau^* = \frac{A_1\tau_1^2 + A_2\tau_2^2}{A_1\tau_1 + A_2\tau_2} \quad (6)$$

As determined at 510 nm, the average lifetimes of the $Ba_{1-x}Ca_xScO_2F:Bi^{3+},K^+$ (x = 0, 0.03, 0.06, 0.09, and 0.11) phosphors are listed in Fig. 3f. The results indicate that the average lifetime τ^* firstly increases from 13.864(2) μs to 16.002(6) μs due to the increase of Bi^{3+} radiation transition with the increase of Ca^{2+} substitution and then the average lifetime τ^* decreases from 16.002(6) μs to 15.539(8) μs due to the increase of non-radiation transition for higher Ca^{2+} substitution.

The schematic energy level diagram of Bi^{3+} ions in the (Ba,Ca)ScO_2F crystal structure is shown in Fig. 4. It is well known that the ground state of Bi^{3+} coming from the $6s^2$ electronic configuration is the $^1S_0$ state. The excited states of Bi^{3+} with the 6s6p configuration are the $^3P_0$, $^3P_1$, $^3P_2$, and $^1P_1$ states, respectively. The transitions from $^1S_0$ to $^3P_0$ and $^3P_2$ are completely spin forbidden. The two energy levels $^3P_1$ and $^1P_1$ are mixed by spin–orbit coupling. Therefore, only the $^1S_0 \rightarrow {}^3P_1$ and $^1S_0 \rightarrow {}^1P_1$ transitions have reasonable absorption strength.[14,42] The luminescence of Bi^{3+} strongly depends on the crystallographic environment in the host lattice. Hence, the two emission peaks from Bi (1) and Bi (2) reveal a red shift because the substitution of the smaller Ca^{2+} induces enhancement of the crystal splitting.

Thermal quenching properties

The thermal stability of the as-prepared phosphors has an important effect on the applications of high-quality w-LEDs.[45–47] Therefore, it is necessary to evaluate the thermal quenching behavior of the as-prepared phosphor. Fig. 5a shows the normalized integrated emission intensities of $Ba_{1-x}Ca_xScO_2F:Bi^{3+},K^+$ (x = 0, 0.06, and 0.12) phosphors from 298 K to 523 K under 415 nm excitation. The temperature-dependent photoluminescence spectra of $Ba_{0.94}Ca_{0.06}ScO_2F:0.001Bi^{3+},0.001K^+$ are displayed in Fig. 5b. As the temperature increases, the integrated emission intensities of all the samples show a decreasing, increasing, and then decreasing tendency. An antithermal quenching phenomenon is discovered in $Ba_{1-x}Ca_xScO_2F:Bi^{3+},K^+$, when the temperature rises to 348–398 K. The redistribution of the population between the $^3P_0$ and $^3P_1$ excited states and the discharge of electrons trapped in defects upon thermal stimulation lead to the enhanced emission intensities at high temperatures.[14] In general, the occurrence of thermal quenching was mainly attributed to the enhancement in nonradiative transition probability. At 423 K, the integrated emission intensities of $Ba_{1-x}Ca_xScO_2F:0.001Bi^{3+},0.001K^+$ (x = 0, 0.06, and 0.12) are about 84.6, 95.6 and 92.1%, respectively, compared to the intensities measured at room temperature (298 K) and this indicates that the thermal stability of the as-prepared phosphor increases with Ca^{2+} doping, showing that the introduction of Ca^{2+} ions makes the structure more rigid and increases the structural distortion relative to that without Ca^{2+} doping. The thermal stability increase can be linked to the improved structure rigidity and enhanced formation of defect levels in the host.[48] To further appraise the structural rigidity of the Ca^{2+}-doped phosphors, Debye temperature for the crystallographically distinct atom ($\Theta_{D,i}$) is calculated from the anisotropic atomic displacement parameters using the following equation:[49,50]

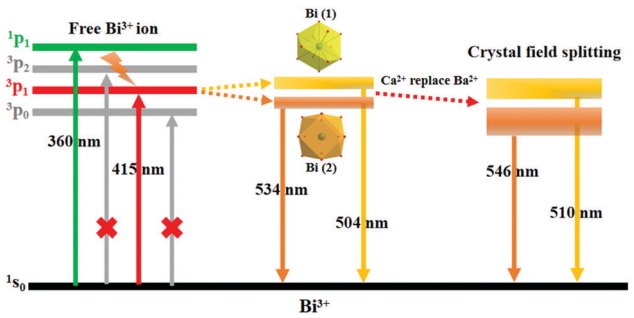

Fig. 4 Schematic energy level diagram for Bi^{3+} ions in the (Ba,Ca)ScO_2F crystal structures.

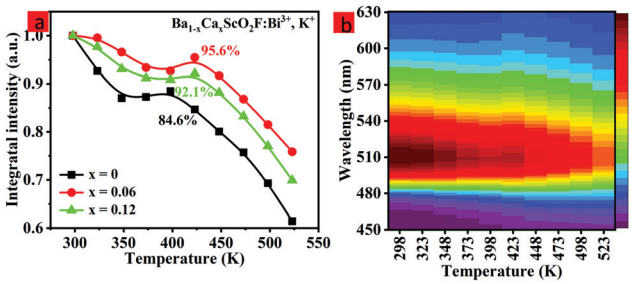

Fig. 5 Temperature-dependent integrated emission intensities of $Ba_{1-x}Ca_xScO_2F:0.001Bi^{3+},0.001K^+$ (x = 0, 0.06, and 0.12) phosphors in the temperature range of 298–523 K (a). The temperature-dependent photoluminescence spectra of the $Ba_{0.94}Ca_{0.06}ScO_2F:0.001Bi^{3+},0.001K^+$ phosphor, as recorded at temperatures ranging from 298 to 523 K under 415 nm NUV excitation (b).

$$\Theta_{D,i} = \sqrt{\frac{3\hbar^2 T N_A}{A_i k_B U_{iso,i}}} \quad (7)$$

where A_i is the atomic weight, k_B is the Boltzmann constant, $\hbar$ represents the Planck constant, $U_{iso,i}$ exhibits the atomic average displacement parameter, and the $\Theta_{D,i}$ is inversely proportional to the value of U_{iso}. The U_{iso} values of $Ba_{1-x}Ca_xScO_2F:Bi^{3+},K^+$ (x = 0, 0.06) were obtained by refinement. The results show that $Ba_{0.94}Ca_{0.06}ScO_2F:Bi^{3+},K^+$ has a U_{iso} of 0.01042, as small as that of $BaScO_2F:Bi^{3+},K^+$ (0.01307), respectively. The results indicate the great rigidity for $Ba_{0.94}Ca_{0.06}ScO_2F:Bi^{3+},K^+$ relative to $BaScO_2F:Bi^{3+},K^+$, which is

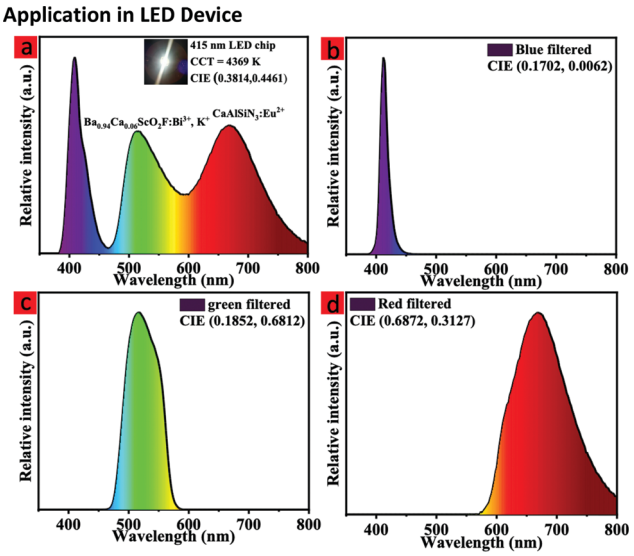

Fig. 6 The EL spectrum of an LED (a). The inset is a working photograph of the LED. The EL spectra of the LED after red, green, and blue color filtering (b–d).

consistent with the above results. The (Ba,Ca)ScO_2F:Bi^{3+},K^+ phosphor shows low thermal quenching at 423 K. In particular, for x = 0.06, at 423 K the intensity remains 95.6% of that at 298 K.

Application in LED device

To further evaluate the backlight display application potential of the $Ba_{0.94}Ca_{0.06}ScO_2F:Bi^{3+},K^+$ phosphors, a w-LED was packaged using a NUV chip (415 nm), the commercial red phosphor $CaAlSiN_3:Eu^{2+}$ and the synthesized green phosphor $Ba_{0.94}Ca_{0.06}ScO_2F:Bi^{3+},K^+$. Fig. 6a and 7 display the emission spectrum and the color gamut of the fabricated W-LED under a 120 mA driving current, and the inset is a working photograph of the LED. The constructed LED produces a white light emission with CIE chromaticity coordinates of (0.3814, 0.4461), a correlated color temperature (CCT) of 4369 K, and luminance efficiency (LE) of 27.00 lm W^{-1}.

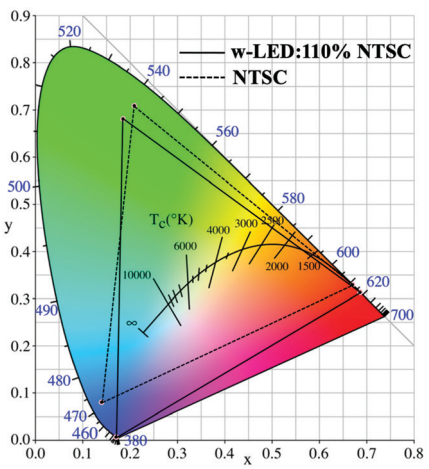

Fig. 7 The color gamut of the LED.

Table 2 Main photoelectric parameters of some reported w-LEDs

Green emitting phosphor	Red emitting phosphor	CCT (K)	The color gamut (% of the NTSC value)	Ref.
YAG:Ce^{3+}	CASN:Eu^{2+}	10 260	80	8
Sr_2SiO_4:Eu^{2+}	CASN:Eu^{2+}	8000	74.7	50
β-Sialon:Eu^{2+}	CASN:Eu^{2+}	8620	82.1	52
$SrGa_2S_4$:Eu^{2+}	CASN:Eu^{2+}	12 723	83.8	50
$Ba_{0.94}Ca_{0.06}ScO_2F:Bi^{3+},K^+$	CASN:Eu^{2+}	4369	110.3	This work

To obtain the color gamut of the LED, conventional commercial color filters were used to filter the white light. The filtered red (R), green (G), and blue (B) EL spectra are shown in Fig. 6b–d, respectively. To further understand the chromatic behaviors of the phosphor, the color purity was calculated according to the following expression:[51,52]

$$\text{Color purity} = \frac{\sqrt{(x-x_i)^2+(y-y_i)^2}}{\sqrt{(x_d-x_i)^2+(y_d-y_i)^2}} \quad (8)$$

In this expression, (x, y) represents the CIE coordinates of $Ba_{0.94}Ca_{0.06}ScO_2F:Bi^{3+},K^+$ green phosphor, (x_i, y_i) represents the chromaticity coordinates of an equal-energy white light source with the values of (0.3333, 0.3333), and (x_d, y_d) stands for the CIE coordinates of the corresponding dominant wavelength of the illuminant. The calculated color purity of the $Ba_{0.94}Ca_{0.06}ScO_2F:Bi^{3+},K^+$ phosphor is about 68.4%, which is conducive to good application prospects in the field of backlight displays. In addition, the color gamut of the fabricated white LED can reach 110.3% of the National Television Standard Committee (NTSC) value.

Table 2 lists some reported WLEDs for LED backlights. On the basis of these photoelectric parameters, it is concluded that the $Ba_{0.94}Ca_{0.06}ScO_2F:Bi^{3+},K^+$ phosphor is an efficient green compensator. The LED with such a wide color gamut and excellent color quality demonstrates potential for applications in backlight displays.

Conclusions

In summary, green emitting $Ba_{1-x}Ca_xScO_2F:0.001Bi^{3+},0.001K^+$ (x = 0–0.12) phosphors with an FWHM of 60 nm were successfully developed for LED backlight displays *via* the cation substitution strategy. All phosphors show the cubic perovskite-type structure with the space group *Pm3m*. With the smaller Ca^{2+} ions substituting Ba^{2+}, the structure shrinkage leads to the increase of the crystal field splitting level, and, further, the luminescence intensity and thermal stabilities of (Ba,Ca)ScO_2F: Bi^{3+},K^+ can be effectively enhanced. The cation substitution design can become an important approach to PL spectral modulation through controlling the ion environment in the crystal lattice. Finally, a w-LED device with the high color gamut of 110% of the NTSC value and a lower CCT of 4369 K was fabricated. The results demonstrate that (Ba,Ca)ScO_2F: Bi^{3+},K^+

is a promising luminescent material, which can be used in LED backlight displays.

Conflicts of interest

There are no conflicts to declare.

Acknowledgements

This work is supported by the National Natural Science Foundation of China (Grant No. 12174042), the Key Program of Technology Innovation and Application of Chongqing (2019jscx-nbdxx0023), the Science and Technology Research Program of Chongqing Municipal Education Commission (KJZD-M201901301) and Fund for Creative Research Group of Fund for Creative Research Group of Micro-Nano Semiconductor & Photonic Materials of Chongqing Municipal Education Commission. Damir Valiev and Elena F. Polisadova appreciate the support from Tomsk Polytechnic University, the Priority 2030 Federal Academic Leadership Program.

Notes and references

1 P. Pust, P. J. Schmidt and W. Schnick, *Nat. Mater.*, 2015, **14**, 454–458.
2 R. Gautier, X. Li, Z. Xia and F. Massuyeau, *J. Am. Chem. Soc.*, 2017, **139**, 1436–1439.
3 H. Daicho, T. Iwasaki, K. Enomoto, Y. Sasaki, Y. Maeno, Y. Shinomiya, S. Aoyagi, E. Nishibori, M. Sakata, H. Sawa, S. Matsuishi and H. Hosono, *Nat. Commun.*, 2012, **3**, 1–8.
4 T. Hashimoto, F. Wu, J. S. Speck and S. Nakamura, *Nat. Mater.*, 2007, **6**, 568–571.
5 Z. G. Xia, Y. Y. Zhang, M. S. Molokeev and V. V. Atuchin, *J. Phys. Chem. C*, 2013, **117**, 20847–20854.
6 H. P. Ji, Z. H. Huang, Z. G. Xia, M. S. Molokeev, V. V. Atuchin, M. H. Fang and S. F. Huang, *Inorg. Chem.*, 2014, **53**, 5129–5135.
7 J. L. Leaño, S. Y. Lin, A. Lazarowska, S. Mahlik, M. Grinberg, C. L. Liang, W. Z. Zhou, M. S. Molokeev, V. V. Atuchin, Y. T. Tsai, C. C. Lin, H. S. Sheu and R. S. Liu, *Chem. Mater.*, 2016, **28**, 6822–6825.
8 L. Wang, R. J. Xie, T. Suehiro, T. Takeda and N. Hirosaki, *Chem. Rev.*, 2018, **118**, 1951–2009.
9 R. J. Xie, H. Naoto and T. Takashi, *Appl. Phys. Express*, 2009, **2**, 022401.
10 H. A. Höppe, *Angew. Chem., Int. Ed.*, 2009, **48**, 3572–3582.
11 J. H. Oh, H. Kang, M. Ko and Y. R. Do, *Opt. Express*, 2015, **23**, A791.
12 K. Yoshimura, K. Annen, H. Fukunaga, M. Harada, M. Izumi, K. Takahashi, T. Uchikoshi, R. Xie and N. Hirosaki, *Jpn. J. Appl. Phys.*, 2016, **55**, 42102.
13 E. H. Song, Y. Y. Zhou, Y. Wei, X. X. Han, Z. R. Tao, R. L. Qiu, Z. G. Xia and Q. Y. Zhang, *J. Mater. Chem. C*, 2019, **7**, 8192–8198.
14 M. S. Cai, T. C. Lang, T. Han, D. Valiev, S. Q. Fang, C. Z. Guo, S. S. He, L. L. Peng, S. X. Cao, B. T. Liu, L. Du, Y. Zhong and E. Polisadova, *Inorg. Chem.*, 2021, **60**, 15519–15528.
15 H. Ji, Z. Huang, Z. Xia, M. S. Molokeev, V. V. Atuchin, M. Fang and Y. Liu, *J. Phys. Chem. C*, 2015, **119**, 2038–2045.
16 H. Ji, Z. Huang, Z. Xia, M. S. Molokeev, V. V. Atuchin and S. Huang, *Inorg. Chem.*, 2014, **53**, 11119–11124.
17 H. Ji, Z. Huang, Z. Xia, M. S. Molokeev, V. V. Atuchin, M. Fang and S. Huang, *Inorg. Chem.*, 2014, **53**, 5129–5135.
18 W. B. Im, Y. Fourré, S. Brinkley, J. Sonoda, S. Nakamura, S. P. DenBaars and R. Seshadri, *Opt. Express*, 2009, **17**, 22673–22679.
19 W. Y. Huang, F. Yoshimura, K. Ueda, Y. Shimomura, H. S. Sheu, T. S. Chan, H. F. Greer, W. Zhou, S. F. Hu, R. S. Liu and J. P. Attfield, *Angew. Chem., Int. Ed.*, 2013, **52**, 8102–8106.
20 Z. Xia, C. Ma, M. S. Molokeev, Q. Liu, K. Rickert and K. R. Poeppelmeier, *J. Am. Chem. Soc.*, 2015, **137**, 12494–12497.
21 K. A. Denault, N. C. George, S. R. Paden, S. Brinkley, A. A. Mikhailovsky, J. Neuefeind, S. P. DenBaars and R. Seshadri, *J. Mater. Chem.*, 2012, **22**, 18204–18213.
22 T. C. Lang, T. Han, S. Q. Fang, J. Y. Wang, S. X. Cao, L. L. Peng, B. T. Liu, V. I. Korepanov and A. N. Yakovlev, *Chem. Eng. J.*, 2020, **380**, 122429.
23 H. P. Ji, L. Wang, M. S. Molokeev, N. Hirosaki, Z. H. Huang, Z. G. Xia, O. M. ten Kate, L. H. Liu and R. J. Xie, *J. Mater. Chem. C*, 2016, **4**, 2359–2366.
24 Q. S. Wu, Y. Y. Li, Y. J. Wang, H. Liu, S. S. Ye, L. Zhao, J. Y. Ding and J. C. Zhou, *Chem. Eng. J.*, 2020, **401**, 126130.
25 Z. Y. Wang, Z. G. Xia, M. S. Molokeev, V. V. Atuchin and Q. L. Liu, *Dalton Trans.*, 2014, **43**, 16800–16804.
26 G. G. Li, C. C. Lin, W. T. Chen, M. S. Molokeev, V. V. Atuchin, C. Y. Chiang, W. Z. Zhou, C. W. Wang, W. H. Li, H. S. Sheu, T. S. Chan, C. G. Ma and R. S. Liu, *Chem. Mater.*, 2014, **26**, 2991–3001.
27 M. S. Cai, S. Q. Fang, T. Han, D. T. Valiev, T. C. Lang, Y. Zhong, C. L. Wang, A. N. Yakovlev and E. F. Polisadov, *J. Mater. Chem. C*, 2020, **8**, 14507–14514.
28 Q. Y. Wang, P. Yuan, T. W. Wang, Z. Q. Yin and F. C. Lu, *Ceram. Int.*, 2020, **46**, 1374–1382.
29 K. A. Denault, J. Brgoch, M. W. Gaultois, A. Mikhailovsky, R. Petry, H. Winkler, S. P. DenBaars and R. Seshadri, *Chem. Mater.*, 2014, **26**, 2275–2282.
30 L. Seijo and Z. Barandiarán, *Opt. Mater.*, 2013, **35**, 1932–1940.
31 W. Baur, *Acta Crystallogr., Sect. B: Struct. Crystallogr. Cryst. Chem.*, 1974, **30**, 1195–1215.
32 S. Hariyani and J. Brgoch, *Chem. Mater.*, 2020, **32**, 6640–6649.
33 S. Q. Fang, T. C. Lang, T. Han, M. S. Cai, S. X. Cao, L. L. Peng, B. T. Liu, Y. Zhong, A. N. Yakovlev and V. I. Korepanov, *J. Mater. Chem. C*, 2020, **8**, 6245–6253.
34 R. D. Shannon, *Acta Crystallogr.*, 1976, **32**, 751–767.
35 Q. F. Li, S. A. Zhang, W. X. Lin, W. F. Li, Y. X. Li, Z. F. Mu and F. G. Wu, *Spectrochim. Acta, Part A*, 2020, **228**, 117755.
36 H. M. Luo, S. A. Zhang, Z. F. Mu, F. G. Wu, Z. G. Nie, D. Y. Zhu, X. Feng and Q. T. Zhang, *J. Alloys Compd.*, 2019, **784**, 611–619.

37 S. X. Guo, S. A. Zhang, Z. F. Mu, F. G. Wu, X. Feng, Q. T. Zhang, J. Q. Feng, D. Y. Zhu and Q. P. Du, *J. Lumin.*, 2019, **206**, 278–283.
38 K. Denault, J. Brgoch, S. Kloß, M. Gaultois, J. Siewenie, K. Page and R. Seshadri, *ACS Appl. Mater. Interfaces*, 2015, **7**, 7264–7272.
39 J. Brgoch, M. Gaultois, M. Balasubramanian, K. Page, B. Hong and R. Seshadri, *Appl. Phys. Lett.*, 2014, **105**, 181904.
40 O. Kate, Z. Zhang, J. Ommena and H. Hintzen, *J. Mater. Chem. C*, 2018, **6**, 5671–5683.
41 M. Tian, Z. Wang, W. Li, C. Wang, J. Cheng, Z. Li, Z. Yang and P. Li, *J. Alloys Compd.*, 2019, **787**, 1004–1014.
42 P. P. Dang, D. J. Liu, G. G. Li, A. A. Kheraif and J. Lin, *Adv. Opt. Mater.*, 2020, **8**, 1901993.
43 X. Qin, X. Liu, W. Huang, M. Bettinelli and X. G. Liu, *Chem. Rev.*, 2017, **117**, 4488–4527.
44 P. Dorenbos, *J. Phys.: Condens. Matter*, 2003, **15**, 4797–4807.
45 P. L. Shi, Z. G. Xia, M. S. Molokeev and V. V. Atuchin, *Dalton Trans.*, 2014, **43**, 9669–9676.
46 Z. G. Xia, Z. H. Huang, V. V. Atuchin, P. Hai and M. Y. Chen, *J. Am. Ceram. Soc.*, 2015, **98**, 3280–3284.
47 H. P. Ji, L. Wang, M. S. Molokeev, N. Hirosaki, R. J. Xie, Z. H. Huang, Z. G. Xia, O. M. ten Kate, L. H. Liu and V. V. Atuchin, *J. Mater. Chem. C*, 2016, **4**, 6855–6863.
48 R. Xie, N. Hirosaki, N. Kimura, K. Sakuma and M. Mitomo, *Appl. Phys. Lett.*, 2007, **90**, 191101.
49 W. Xie, C. Tian, F. Lyu, Z. Wang, C. Zou, F. Kang, H. Dong and G. Sun, *J. Am. Ceram. Soc.*, 2019, **102**, 3488–3497.
50 T. C. Lang, J. Y. Wang, T. Han, M. S. Cai, S. Q. Fang, Y. Zhong, L. L. Peng, S. X. Cao, B. T. Liu, E. Polisadova, V. Korepanov and A. Yakovlev, *Inorg. Chem.*, 2021, **60**, 1832–1838.
51 D. Zhao, S. R. Zhang, Y. P. Fan, B. Z. Liu, Y. N. Li, L. Y. Shi and S. J. Dai, *ACS Sustainable Chem. Eng.*, 2020, **8**, 18992–19002.
52 S. Huang, L. X. Yu, K. L. Peng, Y. J. Zhao, J. D. Wang and M. M. Shang, *J. Am. Ceram. Soc.*, 2021, **104**, 5848–5858.